Prediction of corona and multipactor RF breakdown thresholds using the CEST (Corona Simulation Electron Tool) software.

M Alfonseca[(1)], L. Conde[(2)], J. de Lara[(1)], F. Pérez[(1,3)] and D. Raboso[(4)]

[(1)] Escuela Politécnica Superior. Univ. Autónoma de Madrid 28049 Madrid. Spain.
Email: JdeLara@uam.es , Manuel.Alfonseca@uam.es

[(2)]Departamento de Física Aplicada. ETSI Aeronáuticos. Universidad Politécnica de Madrid 28040 Madrid. Spain
Email: Luis.Conde@upm.es

[(3)]GMV. Isaac Newton 11 P.T.M. Tres Cantos E28760 Madrid. Spain
Email: fpandres@gmv.com

[(4)]ESA-ESTEC. Keplerlaan 1, Postbus 299, 2200 AG Noordwijk. The Netherlands
Email: David.Raboso@esa.int

INTRODUCTION

When the communication equipments of spacecrafts are switched on, the progressive outgassing of the spacecraft systems with the altitude, combined with the presence of free electrons in the local environment create the physical conditions to trigger low pressure electric discharges. These charge avalanches are driven by electrons accelerated by the intense radio frequency (RF) electric field which ionize the neutral gas atoms or molecules remaining in the open spaces of the communication system and also produce the secondary electron emission when hit the walls of the waveguides. These undesirable charge space avalanches dissipate an important fraction of the RF input power and may eventually damage the microwave devices leading to catasthrophic failures in the communication systems. Therefore, the prediction of the electric breakdown thresholds is of paramount importance for the design of RF space systems. The numerical simulations of the RF discharge buildup save expensive laboratory testing and also allow to predict the response to microwaves of materials employed for communication systems.

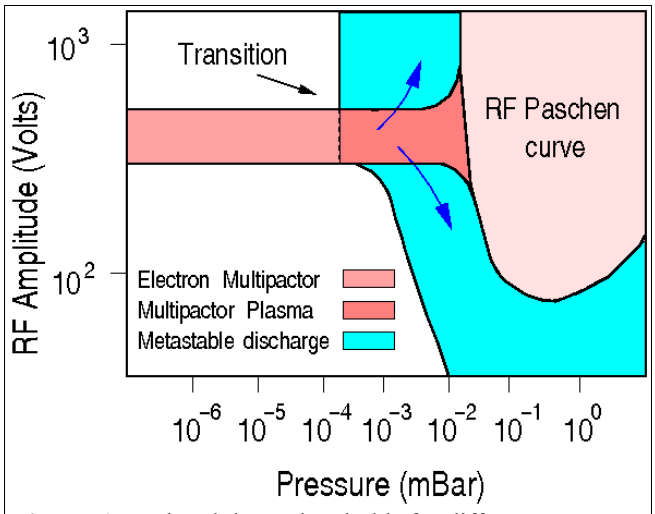

Figure. 1: RF breakdown thresholds for different pressures from the experimental data of Ref. [1].

The RF electric breakdown has been observed in the experiments within a huge range of neutral gas pressures, from 10^{-8} mBar up to 10^{3} mBar. The voltage thresholds for RF discharge breakdown as a function of the neutral gas pressure are shown in Fig. 1 which was obtained from the experimental data of Ref. [1].

In the laboratory experiments the RF microwave discharge is also initiated by seeding electrons originated by cosmic rays or by natural radioactivity which at sea level generates 10^{3} ions by cubic centimeter in steady state at sea level[2]. These electrons are later accelerated by the RF electric field and, in accordance to the neutral gas pressure, two different processes lead the multiplication of charges. The characteristic dimension D of the waveguide, the mean free path λ_{ea} and frequency ν_m for elastic collisions between electrons and neutral atoms lead the different breakdown processes shown in Fig. 2.

For very low pressures, roughly below 10^{-4} mBar $D \gg \lambda_{ea}$ as indicated in the scheme of Fig. 2 and the electrons could hit the walls before the RF electric field reversal. These high energy impacts at the walls of waveguide leads the electrons to be either absorbed, reflected back or to produce the emission of and additional (secondary) electron from the wall. Both are later accelerated by the RF field to produce again additional electrons at the walls. This electron multiplication process is denominated *electron multipactor* and this material dependent RF breakdown is controlled by the secondary electron emission yield $\sigma_{sey}(E)$ which presents a maximum value [2]. The secondary electrons are produced only when the energy E of the colliding lies within the range where $\sigma_{sey}(E)>1$ as evidence the low and high limits for the RF breakdown in Fig. 1 for pressures below 10^{-4} mBar. The thresholds for multipactor have been

successfully predicted by resonant electron models [3]. The buildup and time evolution of this electron discharge have been also studied using particle in cell (PIC), Montercarlo (MP) [4] schemes and more recently, by means of single electron tracking simulations [5].

The opposite limit in Fig. 2 where $D \ll \lambda_{ea}$ corresponds to high pressures (over 10^{-1} mBar) and the involved elastic collision frequencies $\nu_m > f$ are higher than the RF signal frequency *f*. The collisions of electrons with neutral atoms prevent the accelerated electrons from reaching the walls in this case. Because of the high RF electric fields compared with the first ionization energies of neutral gases (in the order of tens of eV) the electrons gain energy enough to produce the electron impact ionization neutral atoms. Thus, new ions and electrons are generated by these inelastic collisions and the charge multiplication process create a *plasma* with positive and negative charges. The secondary emission properties of the material at the walls are in this case of minor relevance and both ions and electrons contribute to the local space charge. The onset for this RF discharge is well described by the classical RF Paschen curves as indicated in Fig. 1 for pressures close to 10^{-1} mBar [2,6].

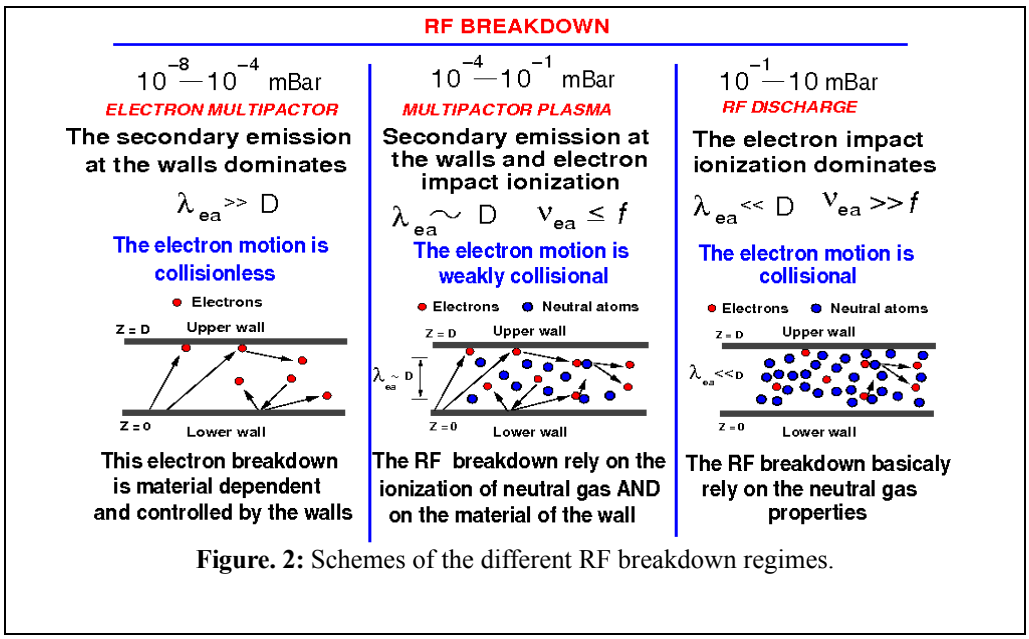

Figure. 2: Schemes of the different RF breakdown regimes.

However, both mechanisms for charge production coexist within the *multipactor plasma* region in Fig. 1 (also denominated *collisional multipactor*) where $D \sim \lambda_{ea}$. The electrons energized by the RF electric field may produce additional charges by both, secondary electron emission and by ionization of neutral atoms. This contribution of electron impact ionization is evidenced in Fig. 1 by the abrupt transition between the *multipactor* and the *multipactor plasma* regions between 10^{-4} and 10^{-2} mBar. Contrary to pure electron multipactor, the electric breakdown does not disappear in the *metaestable regions* when for a fixed gas pressure the RF amplitude is increased or decreased (see arrows in Fig. 1) outside the upper and lower limits corresponding to $\sigma_{sey}(E) > 1$. In the *multipactor plasma* region of Fig. 1 a plasma composed of positive ions and negative charges develops and this fact explains the absence of low and upper bounds for triggering the RF discharge contrary to low pressure electron multipactor. For these intermediate pressures, the electron motion is weakly collisional as shown in Fig 2. Thus, the discharge thresholds found for collisionless multipactor are no longer valid and different refinements have been proposed attempting to incorporate elastic and inelastic collisions into the classical formulations [7,8]. The PIC [9] and MC [10] simulation techniques has been also employed to study this RF breakdown.

The CEST (Corona Electron Simulation Tool) software is intended to predict the RF breakdown thresholds and to simulate the discharge buildup during the time scale of the first cycles of the RF wave. In this particle tracking model the weakly collisional motion of a large number of electrons (up to 2×10^4 particles) is simulated by using of the Langevin stochastic equations of motion in the simplified model for the waveguide of Fig. 3. The simulations cover both, *low pressure multipactor* (below 10^{-4} mBar) and the *collisional multipactor* (roughly from 10^{-4} to 10^{-1} mBar) regions in Fig. 1. The material dependent properties of this RF discharge are also considered through the interaction of electrons with the solid walls which is calculated as in previous MEST (Multipactor Electron Simulation Tool) software for electron multipactor, while the ionizing collisions of electrons with neutral atoms are considered by means of the constant mean free path model.

THE CEST MODEL

The details of the physical model of CEST, its implementation and simulations are described in Ref. [11]. Briefly, the electrons move under the RF field between the parallel metallic walls P and P' of Fig. 3 immersed into a uniform background of neutral gas pressure p_a. Their trajectories are random walks within two infinite parallel walls or alternatively, within the limited test volume $V = D \times H \times D$ of Fig. 3. The force exerted on each electron by the sinusoidal RF electric field pointing along the Z axis is,

$$\boldsymbol{F}_{el} = -e\,\boldsymbol{E}(t) \qquad \text{where} \qquad \boldsymbol{E}(t) = \frac{V_o}{D}\sin(2\pi f t)\;\boldsymbol{k}$$

and two forces account for the electron interaction with the neutral atom background. First, the friction force $\boldsymbol{F}_r = -m_e \nu_m \boldsymbol{u}_e$ represents the resistance to the electron advance in the direction parallel to the electron speed $\boldsymbol{u}_e$ [7]. The elastic collision frequency $\nu_m = \sigma_m n_a u_e$ between electrons and neutral atoms for momentum transfer and rely on the cross section $\sigma_m(E)$ which is obtained from experimental data. In second place, the random scatter of electrons by neutral atoms is introduced by means of a time dependent random force,

$$\boldsymbol{F}_d = \boldsymbol{C} \cdot \boldsymbol{\Gamma} \tag{1}$$

where $\boldsymbol{C}$ is a diagonal matrix and the vector $\boldsymbol{\Gamma}(t)$ a random variable. Because two successive electron collisions are uncorrelated this latter satisfy (Gaussian white noise),

$$\langle \Gamma_i(t) = 0 \rangle \qquad \text{and} \qquad \langle \Gamma_i(t)\;\; \Gamma_j(t') \rangle = \delta_{ij}\,\delta(t - t') \tag{2}$$

Here $\langle \ldots \rangle$ denotes an average over all possible realizations of this variable (*ensemble average*). Because the distribution of neutral atoms is uniform in the test volume of Fig. 1 the dispersion of electrons by elastic collisions is also uniform. In order to reflect this spatial isotropy of the electron scattering, the elements of $\boldsymbol{C}$ in Eq. (1) are independent of the position within the test volume and $C_{ij} = C$ is given by,

$$C = \sqrt{\frac{2 K_B T_e}{m_e}}\sqrt{\nu_m}$$

where $K_b T_e$ is calculated from the average energy $\langle E \rangle$ of electrons present in the simulation. In CEST simulations the following system of stochastic differential equations describe the motion of each electron present in the test volume,

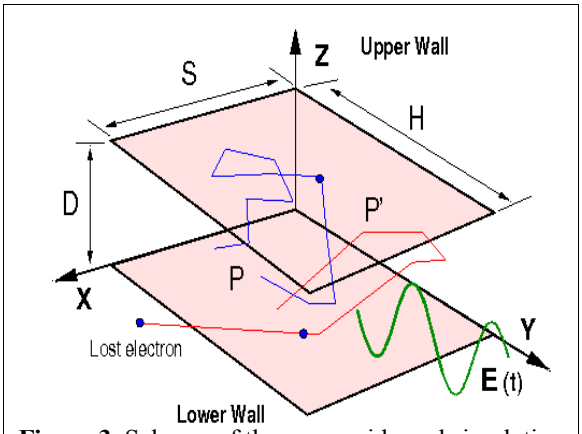

Figure 3. Scheme of the waveguide and simulation volume between the parallel walls P and P'.

$$\frac{d\boldsymbol{r}_e}{dt} = \boldsymbol{u}_e \tag{3}$$

$$\frac{d\boldsymbol{u}_e}{dt} = -\frac{e}{m_e}\boldsymbol{E}(t) - \nu_m \boldsymbol{u}_e + \boldsymbol{C} \cdot \boldsymbol{\Gamma} \tag{4}$$

which are currently denominated *Langevin equations* for the electron motion [12] which have been also used to model the dynamics of charged particle beams [13] and the electron runaway in plasmas [14] .

The equations (3) and (4) are made dimensionless by using D for the length scale and $\tau = t/T$ for time scale where $T = 1/f$ is the period of the RF signal. Thus, $d/dt = f\,d/d\tau$ with $p = x/D$, $q = y/D$ and $r = z/D$ are dimensionless coordinates and the components of the electron speed are,

$$\frac{dp}{d\tau} = U_p = \frac{u_{ex}}{f D} \quad , \qquad \frac{dq}{d\tau} = U_q = \frac{u_{ey}}{f D} \quad , \qquad \frac{dr}{d\tau} = U_r = \frac{u_{ez}}{f D}$$

Finally, we obtain the following dimensionless Langevin equations,

$$\frac{dU_p}{d\tau} = -\frac{\nu_m}{f} U_p + \frac{V_{eT}}{f\,D}\sqrt{\frac{\nu_m}{f}}\;\zeta_p(\tau) \tag{5}$$

$$\frac{dU_q}{d\tau} = -\frac{\nu_m}{f} U_q + \frac{V_{eT}}{f\,D}\sqrt{\frac{\nu_m}{f}}\;\zeta_q(\tau) \tag{6}$$

$$\frac{dU_r}{d\tau} = -\frac{\nu_m}{f} U_r - \frac{1}{2}\left(\frac{V_m}{f\,D}\right)^2 \sin(2\pi\tau) + \frac{V_{eT}}{f\,D}\sqrt{\frac{\nu_m}{f}}\;\zeta_r(\tau) \tag{7}$$

where $V_{eT} = \sqrt{2K_B T_e / m_e}$ and $V_{me}^2 = 2eV_o/m_e$ represents the maximum electron speed. The equations (5) and (6) govern the electron motion along the *X* and *Y* directions in Fig. 3 while Eq. (7) also accounts for the RF sinusoidal electric field along *Z* coordinate with peak amplitude V_o/D. In the above equations $\zeta_p(\tau)$, $\zeta_q(\tau)$ and $\zeta_r(\tau)$ are time dependent dimensionless random variables.

These stochastic dimensionless equations (5-7) rely on the following positive coefficients,

$$a = \frac{\nu_m}{f} \quad , \qquad b = \frac{1}{2}\left(\frac{V_m}{f\,D}\right)^2 \quad \text{and,} \qquad c = \frac{V_{eT}}{f\,D}\sqrt{\frac{\nu_m}{f}} = \frac{V_{eT}}{f\,D}\sqrt{a} \tag{8}$$

The RF peak amplitude V_0, signal frequency *f* and the gap *D* determine the relative weight of each term in the dimensionless equation of motion for electrons. It is of worth to recall that the dimensionless coefficient $a = \nu_{ea}/f$ is related with the time scale of RF signal and was previously discussed in connection to the scheme of Fig. 2.

The values for the parameter a in Eqs. (8) rely on the friction coefficient $\nu_m = n_a \sigma_m(E)\sqrt{2\langle E\rangle/m_e}$ which depends on the neutral gas pressure $(n_a \sim p_a)$ the average electron energy $\langle E\rangle$ and the cross section for momentum transfer $\sigma_m(E)$. This later is obtained from experimental data and depends on the energy *E* of colliding electrons.

For low electron energies the cross sections for momentum transfer present a strong dependence with the energy *E* of the incident electron, in particular below 10 eV the *Ramssauer effect* increments the value of $\sigma_m(E)$ because of the overlapping of quantum wave functions. Nevertheless, the minimum involved peak voltages V_o are in the order of hundred of volts and therefore the typical energy of most electrons in CEST simulations corresponds to smoother values for $\sigma_m(E)$. In consequence, the cross section in the collision frequency $\nu_m(E)$ is approximated by an averaged energy independent value $\sigma_m(E) \sim \sigma_o$.

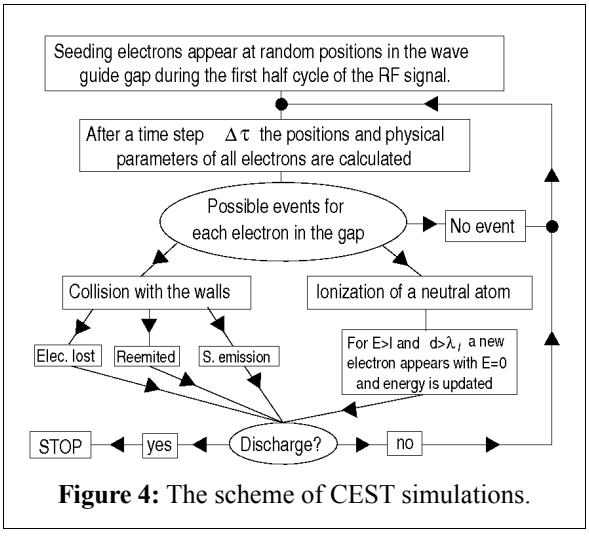

Figure 4: The scheme of CEST simulations.

In this particle tracking model the ionization of the neutral gas could be easily incorporated, contrary to previously mentioned *collisional multipactor* models [7]. The ionizations are produced by electrons energized by the RF electric field and the ionization rate is determined by the corresponding cross section $\sigma_I(E)$. The electron impact ionization process has a threshold with an abrupt growth for electron energies *E* over the first ionization energy E_I of the neutral gas, which lies in the order of tens of eV. Again, because of the high RF electric fields involved, most electrons present in the simulation have energies over E_I where the curves for $\sigma_I(E)$ are smoother.

Therefore, the CEST model considers an energy independent averaged ionization cross section $\sigma_I(E) \sim \sigma_{Io}$ which leads to a constant ionization mean free path $\lambda_I = 1/(\sigma_{Io} n_a)$. For all electrons present in the simulation volume of Fig. 3 the following conditions are checked after each integration step of Eqs. (5-7) of magnitude $\Delta\tau$ in order to determine if an ionization event takes place:

- The electron is located in the gap of Fig. 3.
- The kinetic energy of the electron *E* lies over the first ionization energy $E > E_I$ of the neutral gas.
- The distance *L* covered by each electron after his last ionization event is larger than the ionization mean free path λ_I.

In CEST model the ionizations of neutral atoms are produced by electrons which meet these conditions. In this case, a new electron is created at rest ($E=0$) at the position of the ionizing electron and is incorporated into the electron population. The ionization length L of ionizing electrons is set to $L=0$, its kinetic energy reduced by an amount of E_I and its new speed $\boldsymbol{u}_e$ randomly scattered. In the next time step $\Delta\tau$ both, new and old electrons move under the RF electric field and the produced ions are ignored as in previous models [7].

The velocity and trajectory of each electron present in the simulation are calculated during the dimesionless time τ by the numerically integration of the Eqs. (5-7) by means of a Milstein scheme [15]. This allow to simulate the random motion of electrons by the scattering of neutral gas atoms within the test volume of Fig. 3. The interaction of electrons with the walls is considered as in previous MEST model [5]. Thus, additional electrons are incorporated into the simulation when either, the ionization of a neutral atom or the secondary emission occurs, and are retired when electrons are lost. Because CEST performs a numerical integration of the equations of motion the coefficients (8) need to be of the same order of magnitude. This introduces the limits to the applicability of CEST model discussed in Ref. [11] which depend of the RF signal frequency f, the maximum voltage amplitude V_o, gap size D and neutral gas pressure p_a .

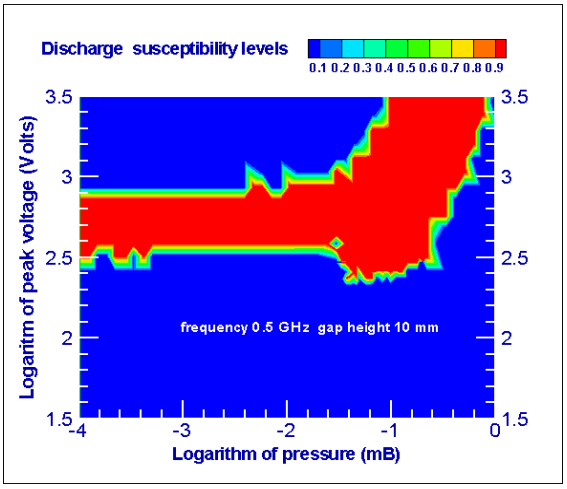

Figure 5. Simulation with CEST for different neutral gas pressures of the RF discharge thresholds of the experimental data of Ref. [1]

The structure of simulations performed by CEST is shown in Fig. 4. First, a seeding population of electrons with a Maxwell Boltzmann energy distribution appear during the first half of the RF signal. These initial electrons move under the RF electric field, are randomly scattered by elastic collisions and also friction with the neutral atom background. Their positions and speeds after a time step $\Delta\tau$ are obtained by the numerical integration of the dimensionless equations (5-7). After the integration step the new positions of particles are checked and for those colliding with the walls the analysis formulated in MEST is performed. These electrons could be lost, re-emitted or an additional particle is incorporated into the simulation. The electrons located far from the walls could continue their motion (no event) or to ionize a neutral gas atom.

Finally, the number of initial and produced electrons is calculated and compared with the electron multiplication rate considered for breakdown. In the event of the number of electrons present exceeds the used defined onset the simulation is stopped. Otherwise, all parameters are calculated again and a new integration step of Eqs. (5-7) is performed. The velocity of growth of the electron population of the electron population defines the so called *susceptibility*,

$$s(\tau)=\frac{d}{d\tau}\ln(N_e(\tau)) \qquad \text{and is approximated by,} \qquad s(\tau+\Delta\tau)=\frac{1}{\Delta\tau}\ln\left(\frac{N_e(\tau+\Delta\tau)}{N_e(\tau)}\right) \qquad (8)$$

This quantity is $s(\tau)\leq 0$ when the initial population of electrons decreases or remains constant and becomes positive in the event for an electron multiplication process. Therefore, the magnitude of this dimensionless magnitude permits to classify the different RF discharge regions.

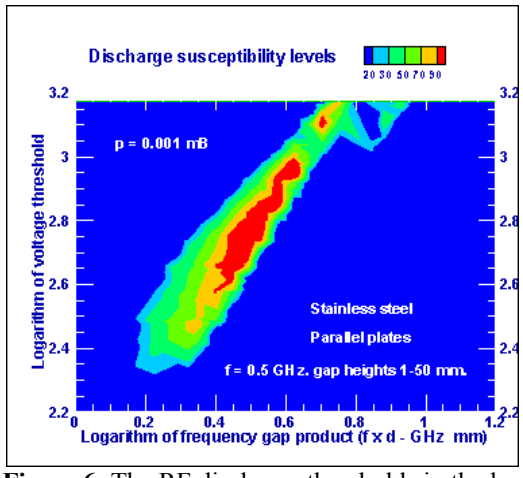

Figure 6: The RF discharge thresholds in the low pressure multipactor region.

RESULTS

The results of CEST simulations have been compared with theoretical predictions and the experimental results from Ref. [1]. In Fig. [4] is represented the RF peak voltage discharge regions calculated with CEST as a function of the neutral gas pressure of Argon which are in good agreement with the experimental data in [1], shown in Fig. 1. The high and low voltage thresholds of Fig. 1 for *multipactor* are reproduced as well as the *multipactor plasma* region. However, the mestastable discharge zones [1] indicated by the arrows in Fig. 1. could not be obtained with CEST as well as the high

pressure region lying over 1 mBar. The collision frequency is proportional to the neutral gas pressure p_a and for pressures where $\nu_m > f$ the elastic collisions confine the motion of electrons which could not reach the walls. Thus, as discussed in [11], in the absence of energy losses, CEST predicts an unrealistic growth of ionizations.

In order to compare with the experimental results for low pressure multipactor and the theoretical simulations with MEST, the RF discharge voltages V_o are represented as a function of the product $f \times D$ of the microwave frequencies f and gap length D. In Fig. 6 is shown this $V_o - f \times D$ map obtained with CEST at the pressure of 10^{-3} mBar of Argon, which in agreement with previous simulations with MEST [5]. Because of the involved low gas pressures the only source of charges is the secondary electron production at the walls of the simulation volume of Fig. 3 in this case.

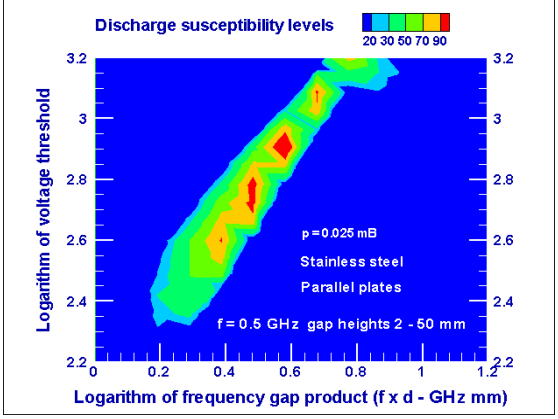

Figure 7: RF discharge in the *multipactor plasma* region

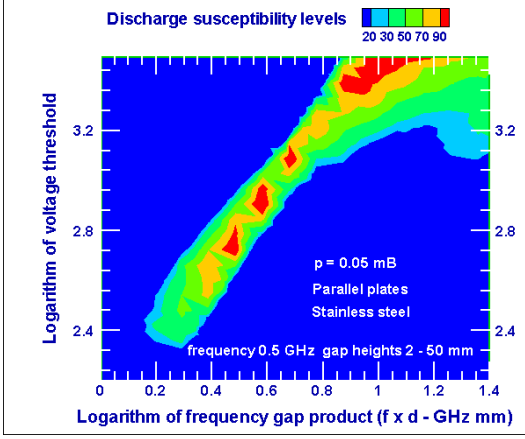

Figure 8: RF discharge in the *multipactor plasma* region in Argon.

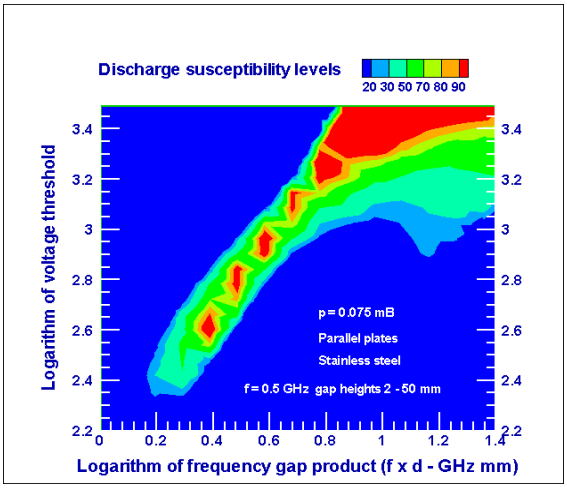

Figure 9: RF discharge in the *multipactor plasma* region in Argon.

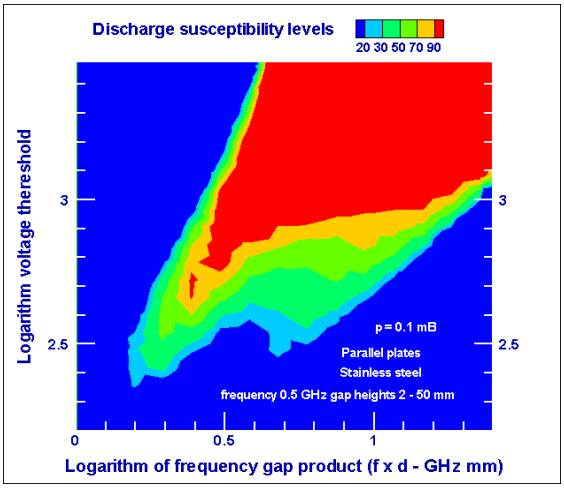

Figure 10: RF discharge in the *multipactor plasma* region in Argon.

The electron impact ionization of the neutral gas becomes important and the CEST simulations as the neutral gas pressure increases. The results within the *multipactor plasma* region are shown in the sequence of Figs. 7-12 where it may be observed that the discharge region becomes displaced towards higher values of $f \times D$. In these figures the discharge zones also becomes thicker and the areas with higher susceptibility levels are broader. These results are similar to those obtained by using improved resonant electron models for collisional multipactor [7].

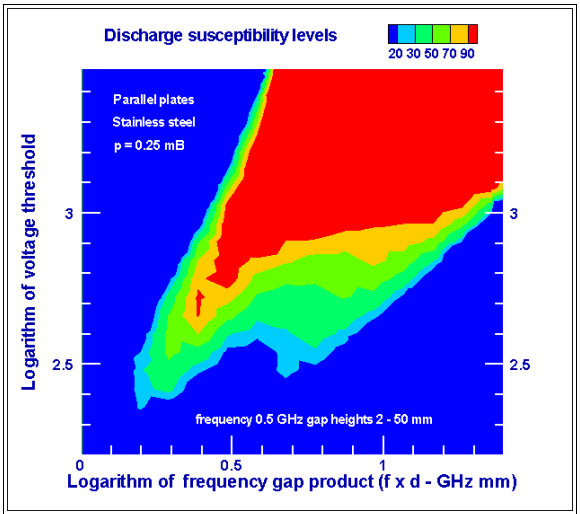

Figure 11: RF discharge in the *multipactor plasma* region in Argon.

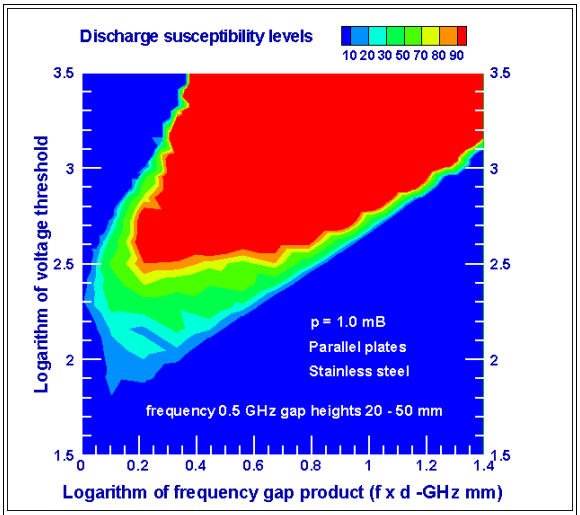

Figure 12: RF discharge in the *multipactor plasma* region in Argon.

Acknowledgements

This work was supported by ESA-ESTEC under program A=4025 ITT ESA entitled *Surface treatment and coating for the reduction of multipactor and passive intermodulation (PIM) effects in RF components*. The authors gratefully acknowledge the support from Tesat Spacecom GmbH, the fruitful discussions with D. Wolk, A.Meinrad and U. Wolchner as well as the suggestions from Prof. L. Galán.

REFERENCES

[1] F. Höhn, W. Jacob, R. Beckmann and R. Whilhelm. "The transition of a multipactor to a low pressure gas discharge". *Phys. Plasmas*, **4**, (10), pp. 940-4111, 1997.
[2] Y.P. Raizer. *"Gas Discharge Physics"*. Springer Verlag, Berlin, 1991.
[3] R.A. Kishek, Y.Y. Lau, L.K. Ang, A. Valfells and R.M. Gilgenbach, "Multipactor discharge on metals and dielectrics: Historical review and recent theories". *Phys. Plasmas*, **5**, (5), pp. 2120-2126, 1998.
Semenov, A. Kryazhev, D. Anderson and M. Lisak. "Multipactor suppression in amplitude modulated radio frequency fields". *Phys. Plasmas* **8**, (11), pp. 5034-5039, (2001). A. Kryazhev, M. Buyanova, V. Semenov, D. Anderson, M. Lisak, J. Puech, L. Lapierre, and J. Sombrin. "Hybrid resonant modes of two-sided multipactor and transition to the polyphase regime". *Phys. Plasmas* **9**, (11), pp. 4736-4743, 2002.
[4] A. Valfells, J.P. Verboncoeur and Y.Y. Lau. "Time dependent physics of a single surface multipactor discharge". *IEEE Trans. Plasma Sci*. **26**, pp. 529-532, 2000. H.C. Kim and J.P. Verboncoeur. " Time dependent physics of a single surface multipactor discharge". *Phys. Plasmas* **12**, (12), 123504, 2005.
[5] J. de Lara, F. Pérez,M. Alfonseca, L. Galán, I. Montero, E. Román and D. Raboso. "Multipactor prediction for on-board spacecraft RF equipment with the MEST software tool". *IEEE Trans. on Plasma Sci*. **34**, (2), pp. 476-484, 2006.
[6] A.E.D. Heylen. "Sparking formulae for very high voltage Paschen characteristics of gases". *IEEE Electrical Insulation Magazine*, **22**, (3), pp. 25-35, 2006. A.E.D. Heylen and V. Postoyalko. "Calculated microwave breakdown voltages in nitrogen, oxigen and air from DC data". *Int. J. of electronics*. **71**, (4), 707-713, 1991.
[7] R. Udiljak, D. Andersson, M. Lisak, V.E. Semenov and J. Puech. "Multipactor in low pressure gas". *Phys. Plasmas*, **10**, (10), pp. 4105-4111, 2003. R. Udiljak, D. Andersson, M. Lisak, V.E. Semenov and J. Puech. "Improved model for multipactor in low pressure gas". *Phys. Plasmas*, **11**, (11), pp. 5022-5031, 2004.
[8] S. Riyopoulos. "Collisional multipactor inside ambient gas". *Phys. Plasmas*, **11**, (5), pp. 2036-2045, 2004.
[9] D. Vender, H.B. Smith and R.W. Boswell. " Simulations of multipactor assisted breakdown in radio frequency plasmas". *J. Appl. Phys*. **80**, (8), pp. 4292-4298, 1996.
[10] A. Gilardini. "The radiofrequency breakdown in low pressure argon". *J. Phys. D: Appl. Phys.* **32**, pp. 1281-1286, 1999.

[11] F. Pérez, J. de Lara, L. Conde, M. Alfonseca, L. Galán and D. Raboso. “CEST and MEST: Tools for the simulation of radio frequency electric discharges in waveguides”. Manuscript submitted to *Simulation Modelling Practice and Theory*.

[12] C.W. Gardiner. *“Handbook of stochastic methods for Physics, Chemistry and the natural sciences”*. 2nd Edition. Springer Verlag. Berlin 1985.
[13] J. Quiang and S. Habib. “A second order stochastic leap-frog algorithm for multiplicative noise Brownian motion ”. *Phys. Rev. E* **62**, (5), pp. 7430-7437, 2000. J. Quiang and S. Habib. “Self consistent Langevin simulation of Coulomb collisions in charged particle beams”. Proceedings of the XX ACM/IEEE conference on supercomputing. Article no. 27, 2000.
[14] A.G. Zhidkov. “Simulation of electron runaway in a plasma by Langevin equation”. *Phys. Plasmas.* **5**, (2), pp. 385-389, 1998.
[15] D.J. Higham. “An algorithmic introduction to numerical simulation of stochastic differential equations”. *SIAM Review,* **43**, (3), pp. 525-546, 2001.